Research Square

Preprints are preliminary reports that have not undergone peer review.
They should not be considered conclusive, used to inform clinical practice,
or referenced by the media as validated information.

Waste Coconut Shell-Derived Nitrogen-Doped Porous Carbon Synergized with Bi 2 MoO 6 for Sensitive Detection of Marbofloxacin in Complex Matrices

Yuan Jin
Hunan University of Technology
Junyuan Song
Hunan University of Technology
Nanke Ma
Hunan University of Technology
Yonghui Xia
Zhuzhou Institute for Food and Drug Control
Guangli Li
guangli010@hut.edu.cn

Hunan University of Technology

Research Article

Keywords: Marbofloxacin detection, electrochemical sensor, Bi2MoO6, waste-derived porous carbon, antibiotic monitoring

Posted Date: April 27th, 2026

DOI: https://doi.org/10.21203/rs.3.rs-9392435/v1

License: This work is licensed under a Creative Commons Attribution 4.0 International License.
Read Full License

Additional Declarations: No competing interests reported.

Version of Record: A version of this preprint was published at Microchimica Acta on June 10th, 2026.
See the published version at https://doi.org/10.1007/s00604-026-08183-4.

Abstract

Marbofloxacin (MAR) residues in aquatic environments present a significant threat to both ecological systems and human health. This study presents a novel nanocomposite for the detection of trace MAR, integrating bismuth molybdate (Bi_2MoO_6) with environmentally friendly and cost-effective nitrogen-doped porous biomass carbon (NC), which exhibits high catalytic activity. The NC, derived from waste coconut shells, possesses a high BET specific surface area of 842.72 m^2 g^{-1}, offering a hierarchical pore structure for efficient adsorption and electron transport. Bi_2MoO_6 microsphere uniformly anchored to the NC porous framework, resulting in a collaborative sensing interface characterized by “adsorption-enrichment-catalysis”. In this configuration, NC facilitates rapid electron transport and concentrates target molecules, while Bi_2MoO_6 offers abundant catalytic sites. The resulting Bi_2MoO_6/NC/GCE sensor demonstrates outstanding performance for MAR detection, with a linear range of 0.03 − 10 μM, a sensitivity of 7.958 μA μM^{-1}, and a detection limit of 0.0045 μM. Additionally, the sensor exhibits high selectivity, good reproducibility, and stability, successfully detecting trace levels of MAR in tap water and milk, with recoveries ranging from 96.0% to 100.6%. This study offers an efficient and environmentally friendly approach for the rapid and reliable detection of trace antibiotics in complex matrices.

1. Introduction

Marbofloxacin (MAR), a commonly utilized fluoroquinolone antibiotic, presents a significant threat to ecological security and public health due to its persistent residues in aquatic environments [1–2]. Even minimal concentrations of MAR can markedly inhibit algal photosynthesis, disrupt the primary productivity of aquatic ecosystems, and bioaccumulate through the food chain, thereby jeopardizing ecological balance [3–4]. The enduring presence of MAR strongly promotes the proliferation and horizontal transfer of antibiotic resistance genes, such as qnrS, which diminishes clinical efficacy [5–6]. Furthermore, MAR exhibits pronounced bioaccumulation properties, with concentrations in fish potentially reaching hundreds of times higher than environmental levels [7–9]. Consequently, it poses risks to human health via the food chain, increasing the likelihood of drug-resistant bacterial infections and unknown toxicological hazards [10–11]. Therefore, the development of rapid, sensitive, and reliable environmental monitoring technologies for MAR is crucial for assessing ecological risks, mitigating the spread of drug resistance, and ensuring the safety of drinking water and food.

Currently, the trace detection of MAR primarily depends on traditional methods, including high-performance liquid chromatography (HPLC), spectrophotometry, and fluorescence analysis [12–13]. However, these techniques exhibit significant limitations in fulfilling the requirements for rapid and cost-effective on-site screening [14]. HPLC offers high sensitivity, but it involves expensive instruments, a complex process, and reliance on large-scale equipment, which hinders its on-site applicability [15–16]. Spectrophotometry, while accessible, suffers from relatively low sensitivity and selectivity, making it susceptible to interference from complex samples [17–18]. Fluorescence analysis demonstrates better sensitivity. However, its signal is easily influenced by environmental factors and water composition,

resulting in poor stability [19–20]. In contrast, electrochemical analysis technology presents notable advantages, including simple equipment, rapid response, low cost, high sensitivity, and ease of miniaturization, positioning it as a promising approach for on-site detection [21–22]. Nonetheless, MAR itself exhibits low electrochemical activity, leading to weak responses from sensors utilizing bare electrodes, which restricts its direct application [23–24]. Thus, developing electrode materials with high catalytic activity and selectivity, and building ultra-sensitive electrochemical interfaces, is crucial for rapid and reliable trace MAR detection in the environment.

To enhance the electrocatalytic oxidation performance of MAR, selecting catalyst materials with high intrinsic activity is essential [25–26]. Among various materials, polymetallic oxides typically demonstrate superior catalytic site density and cycling stability compared to single-metal oxides, owing to their unique complementary valence states and stable crystal structures [27–29]. Notably, bismuth molybdate has garnered significant attention in the fields of photoelectrocatalysis and sensing due to its distinctive layered structure, appropriate band position, and the synergistic effects of Bi^{3+} and Mo^{6+} [30–31]. However, pure-phase Bi_2MoO_6 nanomaterials encounter two primary challenges in practical applications [32]. Bi_2MoO_6 nanoparticles (NPs) tend to agglomerate, leading to a substantial reduction in the effective specific surface area and the exposure of active sites [33–34]. The intrinsic electronic conductivity is moderate, which limits the kinetics of the electrocatalytic reaction [35]. To mitigate these issues, an effective strategy involves combining Bi_2MoO_6 with highly conductive carbon materials [36]. By constructing heterojunctions, conductive carbon materials can serve as dispersion carriers to prevent the agglomeration of Bi_2MoO_6 NPs and ensure the full exposure of active interfaces [37–38]. Additionally, they can establish three-dimensional conductive networks, significantly enhancing the overall charge transport capacity of the composite [39].

Nitrogen-doped porous biochar, derived from waste biomass like coconut shells through high-temperature carbonization and chemical activation with KOH, stands out as a superior conductive carrier [40]. This material boasts a unique structure with rich multi-level pores (micropores and mesoporous pores), offering a vast specific surface area that facilitates the uniform dispersion of Bi_2MoO_6 NPs and efficient adsorption of MAR molecules, acting as a nano-concentrator [41–43]. Despite the limited electrocatalytic oxidation capacity of pure nitrogen-doped porous biochar for MAR, combining it with Bi_2MoO_6 NPs aims to synergize their strengths [44]. Nitrogen-doped biochar provides a large specific surface area, rapid electron transport pathways, and extra adsorption sites, while Bi_2MoO_6 NPs contribute highly active catalytic sites, resulting in a high-performance sensing interface that integrates adsorption, enrichment, and catalysis.

In this study, Bi_2MoO_6/nitrogen-doped porous biochar composites were innovatively designed and fabricated, marking their first application as sensitive interfaces for the construction of highly sensitive and selective MAR electrochemical sensors. This composite electrode exhibits exceptional comprehensive sensing performance. Under optimized conditions, the detection of MAR demonstrates a wide linear range, high sensitivity, and a low detection limit. Additionally, this sensor displays outstanding

selectivity, along with good reproducibility, repeatability, and long-term stability. In practical sample testing, the sensor was successfully employed for the detection of MAR in spiked tap water and milk, achieving excellent accuracy and precision. This study not only presents a novel method with superior performance and controllable costs for the trace detection of MAR but also offers valuable insights for designing advanced electrochemical sensing platforms aimed at monitoring pollutants in complex matrices.

2. Materials and methods

2.1 Materials and chemicals

Hydrochloric acid (HCl), bismuth nitrate ($Bi(NO_3)_3 \cdot 5H_2O$), sodium molybdate (Na_2MoO_4), sodium dihydrogen phosphate (NaH_2PO_4), and disodium hydrogen phosphate (Na_2HPO_4) were obtained from Shanghai Aladdin Biochemical Technology Co., Ltd., China. Potassium chloride (KCl), potassium tetrachloroferrate ($K_4[Fe(CN)_6]$), potassium tricyanoferrate ($K_3[Fe(CN)_6]$), anhydrous ethanol, and ethylene glycol were sourced from Sinopharm Chemical Reagent Co., Ltd. (Shanghai, China). The nitrogen-doped porous biochar (NC) materials were supplied by Nanjing XFNANO Materials Technology Co., Ltd., China. All drugs and reagents utilized were of analytical grade and employed without further purification. The experiment utilized deionized water (resistivity: 18.2 MΩ cm), prepared via the same ultrapure water system. Precise quantities of disodium hydrogen phosphate (NaH_2PO_4), potassium hydrogen phosphate (K_2HPO_4), potassium chloride (KCl), and sodium chloride (NaCl) were dissolved in deionized water to yield a 0.1 M phosphate buffered saline (PBS). Subsequently, a small amount of 1 M sodium hydroxide or hydrochloric acid was added to adjust the pH.

2.2 Characterization

The surface morphologies of Bi_2MoO_6, NC, and Bi_2MoO_6/NC composites were characterized using a Zeiss Sigma 300 field emission scanning electron microscope (Zeiss, Germany). The crystal structures of these three materials were analyzed through powder X-ray diffraction (Shimadzu XRD-6100, Japan) employing monochromatic Cu Kα radiation (λ = 0.1541 nanometers, 40 kV, 25 mA). The elemental composition of Bi_2MoO_6/NC was examined using a Thermo Fisher Scientific Nexsa X-ray photoelectron spectrometer (USA) equipped with a monochromatic aluminum Kα X-ray source (1486.6 eV).

2.3 Preparation of nitrogen-doped activated carbon

Coconut shells were initially selected as biomass raw materials and underwent a series of pretreatment steps. These included cleaning to eliminate impurities, drying in an oven at 105°C until a constant weight was achieved, and subsequently crushing and sieving to a particle size of 100–200 mesh to ensure uniformity. The processed biomass was then uniformly mixed with a nitrogen source, specifically melamine, in a mass ratio of 1:1. This mixture was placed in a tube furnace, where it was heated under a nitrogen-protected atmosphere at a rate of 5°C/min to a temperature range of 500–700°C for carbonization, maintaining the temperature for 1–2 hours to produce a nitrogen-doped carbon precursor.

Following carbonization, chemical activation was performed. The carbonized products were soaked and stirred in deionized water with KOH as an activator in a mass ratio of 1:2 for 12 hours. Afterward, the samples were dried and heated to 700–900°C at a rate of 5°C/min in a nitrogen atmosphere for an additional 1–2 hours to generate the pore structure and incorporate nitrogen atoms. Post-activation, the samples were repeatedly washed with dilute HCl and deionized water until neutral to eliminate residual impurities. Finally, the products are dried at 105°C for 12 hours, ground, and sieved to yield nitrogen-doped activated carbon (NC) with a high specific surface area. Throughout this process, it is crucial to strictly control temperature, time, and atmosphere to ensure uniform nitrogen doping and optimize the performance of the activated carbon.

2.4 Preparation of Bi_2MoO_6 and Bi_2MoO_6/NC composite

1.5279 g of $Bi(NO_3)_3 \cdot 5H_2O$ and 0.3247 g of Na_2MoO_4 were weighted into a small beaker. 5 mL of ethylene glycol was added to dissolve the reagents, and the mixture was stirred for 1 h. Subsequently, 20 mL of was deionized water introduced incrementally. The resulting clear solution was transferred to a stainless-steel autoclave and subjected to a reaction at 160°C for 16 h. After completion of the reaction, the solution was allowed to cool to room temperature. The precipitate was washed multiple times with ethanol and then dried at 60°C for 12 h to obtain microspherical Bi_2MoO_6 NPs.

Bi_2MoO_6/NC composite was prepared via a straightforward ultrasonic method. Specifically, 1 mg Bi_2MoO_6 and 1 mg NC powder were dispersed in 2 mL deionized water, followed by 30 minutes of ultrasonic to form a homogenous Bi_2MoO_6/NC dispersion. Prior to each use, the composite dispersion was re-dispersed under 15 minutes of ultrasonication to ensure homogeneity.

2.5 Preparation of Bi_2MoO_6/NC/GCE

A glass carbon electrode (GCE, 3 mm diameter) was sequentially polished to mirror-smooth finish using aqueous slurries of α-Al_2O_3 with particle sizes of 0.3 μm and 0.05 μm on a grinding pad. During polishing, the electrode was held vertically and moved in a circular motion. After each polishing, the electrode surface was thoroughly rinsed with deionized water, and allowed to dry under an infrared lamp.

The Bi_2MoO_6/NC/GCE was fabricated by a conventional drop-casting method (Scheme 1). Using a micropipette with 0.1 μL accuracy, 5 μL of the well-dispersed composite was drop-cast onto the center of the vertically held bare GCE. The modified electrode was then dried under an infrared lamp to form a uniform sensing film, yielding the final Bi_2MoO_6/NC/GCE sensor. For comparative analysis, the Bi_2MoO_6/GCE and NC/GCE were fabricated by the same procedure except for the dispersion used.

2.6 Electrochemical tests

All electrochemical measurements were performed using a CHI 660B electrochemical workstation (Shanghai Chenhua instrument Co. Ltd.), which featured a standard three-electrode system comprising a saturated calomel electrode (SCE) as the reference electrode, a platinum wire as the counter electrode,

and Bi_2MoO_6/NC/GCE as the working electrode. To evaluate the electrode performance, cyclic voltammetry (CV) and electrochemical impedance spectroscopy (EIS) measurements were executed in a 10 mL mixed solution consisting of 0.5 mmol L^{-1} $[Fe(CN)_6]^{3-/4-}$ and 0.1 mol L^{-1} KCl. For CV measurements, the potential was scanned within − 0.2 to 0.6 V at a scan rate of 0.1 V s^{-1}. EIS measurements were conducted at an open-circuit potential across a frequency range of 100,000 to 0.1Hz, applying an alternating current disturbance amplitude of 5 mV. To enhance MAR adsorption on electrode surface, an accumulation treatment at 0 V was performed for 180 s before electrochemical detection. Quantitative analysis of MAR was carried out using linear scanning voltammetry (LSV) within a voltage range of 0 to 1.2 V, with a scan rate of 0.05 V s^{-1}. Prior to each measurement, electrode activation was achieved by executing 20 consecutive CV cycles in blank PBS (pH 6.0). Unless otherwise specified, 0.1 M phosphate buffered saline (PBS, pH 6.0) served as the supporting electrolyte throughout the experiment.

3. Results and discussion

3.1 Characterization of Bi_2MoO_6/NC

The morphology and elemental composition of Bi_2MoO_6, NC, and Bi_2MoO_6/NC composites were characterized using scanning electron microscopy (SEM). As illustrated in Fig. 1A, pristine Bi_2MoO_6 NPs display a characteristic flower-like microsphere morphology, which is self-assembled from two-dimensional nanosheets. The hierarchical and open porous architecture promotes a high specific surface area on the electrode surface, thus increasing the exposure of electroactive sites [45]. Figure 1B reveals that NC possesses a distinct layered etching structure, resulting from the biomass carbonization and activation process [46]. Its abundant pores and interlayer spaces serve as an ideal substrate for the attachment of Bi_2MoO_6 NPs [47]. Figure 1C demonstrates that Bi_2MoO_6 NPs are uniformly anchored to the NC surface without significant agglomeration, resulting in a well-defined heterogeneous composite structure. As shown in Figs. 1D-I, C, Bi, O, Mo, and N elements were uniformly distributed within the Bi_2MoO_6/NC composite, confirming the successful combination of Bi_2MoO_6 and NC. The flower-like microsphere structure of Bi_2MoO_6, comprising self-assembled two-dimensional nanosheets with open and hierarchical pores and high specific surface area, facilitates exposure of electroactive sites [48]. Meanwhile, the layered etching structure of NC, rich in pores and interlayer spaces, acts as a carrier for uniform anchoring and dispersion of Bi_2MoO_6, enhancing the material's overall specific surface area and porosity [49]. This design promotes reactant diffusion and mass transfer by improving accessibility to active interfaces, charge transport efficiency, and structural stability. Consequently, it significantly enhances the sensitivity, response speed, and stability of electrochemical sensing.

Figure 2A shows the X-ray diffraction (XRD) patterns of Bi_2MoO_6, NC and Bi_2MoO_6/NC. The XRD pattern indicates that NC displays a broad and faint diffraction peak at around 26.6°, corresponding to the (002) plane of graphitic carbon structure [50]. Bi_2MoO_6 NPs exhibit distinct diffraction peaks at 2θ of 28.3°,

32.8°, 46.8°, and 55.6°, which can be indexed to (131), (151), (202), (331) crystal facets, respectively (JCPDS No.76-2388) [51]. Moreover, the characteristic diffraction peaks of Bi_2MoO_6 NPs retained in the Bi_2MoO_6/NC, suggesting that the introduction of NC has not altered the primary lattice structure, thereby preserving the inherent catalytic activity of the material [52]. The slight increase in the half-width of certain diffraction peaks may be attributed to the amorphous coating of NC or grain refinement, contributing to the enhancement of surface-active site density.

X-ray photoelectron spectroscopy (XPS) analysis further revealed the chemical state of the surface (Figs. 2B-F). The C 1s signal in the survey spectrum was significantly enhanced, confirming the successful loading of NC. The peaks at 284.8 eV, 286.5 eV and 289.5 eV in the high-resolution C 1s spectrum correspond to C-C, C-O and C-N bonds respectively, indicating that NC introduces nitrogen-containing active functional groups while providing a conductive network [54]. The high-resolution spectra of Mo 3d (~ 232.4 eV and ~ 235.5 eV) and Bi 4f (~ 159.0 eV and ~ 164.3 eV) show that the chemical states of Mo^{6+} and Bi^{3+} remain stable after recombination, ensuring the integrity of the electronic structure of the catalytic center. Particularly importantly, the relative content of the surface hydroxyl (-OH) component located at ~ 531.8 eV in the O 1S spectrum has significantly increased, greatly enhancing the hydrophilicity and surface oxygen-rich properties of the material [55].

The nitrogen adsorption-desorption isotherms and pore size distribution curves (Figs. 2G-H) illustrate significant differences in the pore structures of Bi_2MoO_6 and Bi_2MoO_6/NC. Pristine Bi_2MoO_6 (Fig. 2G) displays typical type IV isotherms and H_3 type hysteresis loops, confirming its mesoporous structure. The BET specific surface area measures only 24.11 $m^2\ g^{-1}$, with an average pore diameter of approximately 40 nm. In contrast, the isotherms of the Bi_2MoO_6/NC composite (Fig. 2H) exhibit a pronounced increase in adsorption capacity in the low-pressure region, accompanied by a distinct hysteresis loop, indicating a rich hierarchical structure of micropores and mesopores. The BET specific surface area of this composite reaches an impressive 842.72 $m^2\ g^{-1}$, with a micropore volume of 0.42 $cm^3\ g^{-1}$. The pore size distribution is concentrated within the micropore range (0.4 – 1.2 nm) and extends into the mesoporous region, with an average pore size of approximately 7 nm as determined by the BJH method. The high specific surface area and hierarchical pore structure offers numerous adsorption sites and facilitate rapid mass transfer pathways for MAR molecules. Concurrently, the three-dimensional conductive network of NC enhances electron transport, while Bi_2MoO_6 NPs, uniformly anchored within the pores, maximally exposes the catalytic active centers.

3.2 Optimization of analytical parameters

To attain optimal electrochemical performance, this study systematically optimized the preparation and detection conditions of the composite materials (Fig. 3A). The findings indicate that the ideal mass ratio of Bi_2MoO_6 to NC is 1:5, at which the composite material achieves an optimal balance of electrical conductivity, catalytic activity, and adsorption performance. The recommended volume for electrode modification is 6 μL, as this quantity produces a uniform, dense, and appropriately thick catalytic film, thereby ensuring high-response signals and interface stability (Fig. 3B). Furthermore, the optimal

accumulation potential is set at 0 V, facilitating the adsorption of MAR on the electrode surface. The accumulation time was established at 180 s, which not only allows for effective adsorption of the target substance but also prevents signal growth from being hindered by saturation of the active sites(Fig. 3C-D). Collectively, these optimized conditions ensure the sensor's high sensitivity and stable response.

As shown in Fig. 3E, the oxidation peak potential shifts negatively with increasing pH, indicating that MAR oxidation involve proton transfer. The maximum oxidation peak current (16.41 μA) was attained at pH 6.0 (Fig. 3F). Consequently, pH 6.0 was identified as the optimal detection condition. The slope of the linear plot of oxidation potential versus buffer pH (approximately − 45 mV/pH), closely aligns with the theoretical value of − 59 mV/pH. This indicates that the electrooxidation of MAR involves an equal number of protons and electrons transferred during the process.

3.3 Electrooxidation mechanism of MAR

To elucidate the electrooxidation mechanism of MAR, LSV curves of 1.0 μM MAR were recorded on Bi_2MoO_6/NC/GCE in 0.1 M PBS (pH 6.0) at various scan rates. As illustrated in Fig. 4A, an increase in the scanning rate (v) leads to a significant increase in the oxidation peak current (i_{pa}), while the oxidation peak potential (E_{pa}) shows a slight positive shift. Moreover, no distinct reduction peak were observed, indicating an irreversible redox process for MAR. Figure 4B demonstrates a strong linear relationship between i_{pa} and v in the range of 25–200 mV s^{-1}, described by the regression equation $i_{pa} = 0.157v - 0.0098$ ($R^2 = 0.9913$). The linear dependence suggests that the electrode reaction is predominantly adsorption-controlled. Although a linear trend is also observed between i_{pa} and $v^{1/2}$ (Fig. 4C), implying some influence from mass transfer within a limited range. The slope of 0.958 obtained from the plot of lgi_{pa} versus lg$v$ (Fig. 4D) closely approximates the theoretical value of 1.0 for surface-confined process. This further confirms that the oxidation of MAR is mainly governed by adsorption. The linear correlation between E_{pa} and ln$v$ follows the Laviron equation for an irreversible system: $E_{pa} = E^{\theta} + (RT/\alpha n\mathrm{F})\ln(RTk^0/\alpha nF) + (RT/\alpha n\mathrm{F})\ln v$, where E^{θ} represents the formal potential, α is the charge transfer coefficient, n is the number of electron transferred, F is the Faraday constant (96480 C mol^{-1}), R is the gas constant (8.314 J K^{-1} mol^{-1}), T is the temperature (298 K), k^0 is the standard rate constant, and v is the scan rate (Fig. 4E). From the slope of the fitted line: $E_{pa} = 0.0382 \ln v + 0.7551$ ($R^2 = 0.9051$), n is calculated to be 2, indicating a two-electron transfer process. Combined with earlier pH-dependent potential shifts, it is concluded that the overall oxidation process of MAR involves the transfer of two electrons and two protons. Based on the foregoing analysis, a proposed electrochemical oxidation mechanism of MAR at the Bi_2MoO_6/NC/GCE is depicted in Fig. 4F. The reaction proceeds via a concerted two-electron, two-proton transfer, with H_2O serving as the oxygen source. Notably, oxidation occurs selectively at the tertiary amine nitrogen of the piperazine ring to yield the corresponding N-oxide, while the quinolone core, the C6-fluoro, C3-carboxyl, and morpholine substituents remain unchanged [55]. This high site selectivity originates from the electron-rich nature of the tertiary amine nitrogen and is further promoted by the catalytic specificity of the Bi_2MoO_6/NC electrode, providing a molecular foundation for the highly selective electrochemical detection of MAR.

3.4 Electrochemical properties of Bi_2MoO_6/NC/GCE

To evaluate the electrochemical performance of the different modified electrodes, CV curves were recorded in 0.5 mmol L^{-1} $[Fe(CN)_6]^{3-/4-}$ redox probe solution (Fig. 5A). For the bare GCE, the anodic peak current (i_{pa}) and cathodic peak current (i_{pc}) were 139.7 μA and 136.4 μA, respectively. Modification with Bi_2MoO_6 NPs resulted in a slight increase in redox peak currents (i_{pa} = 158.4 μA, i_{pc} = 156.1 μA), attributed to its intrinsic electrocatalytic activity. However, agglomeration of Bi_2MoO_6 NPs limited the full exposure of the electroactive sites. The NC-modified GCE exhibited enhanced redox peak currents (i_{pa} = 171.1 μA, i_{pc} = 168.7 μA), benefiting from its porous architecture that facilitates mass transport. Notably, Bi_2MoO_6/NC/GCE delivered the highest redox peak currents (i_{pa} = 230.2 μA, i_{pc} = 228.1 μA). This significant enhancement is ascribed to the three-dimensional network structure of NC, which effectively disperses and immobilizes Bi_2MoO_6 NPs, forming interconnected conductive pathway that substantially increase the electrochemically active surface area. These results demonstrate a pronounced synergistic effect between Bi_2MoO_6 and NC. Furthermore, the effective electroactive surface areas of the various electrodes were estimated using the Randles-Sevcik equation for a reversible process. The calculated effective electroactive surface areas were 0.0843 cm^2 for bare GCE, 0.0955 cm^2 for Bi_2MoO_6/GCE, 0.1032 cm^2 for NC/GCE, and 0.1388 cm^2 for Bi_2MoO_6/NC/GCE. Compared to bare electrodes and single-component modified electrodes, Bi_2MoO_6/NC/GCE exhibited the highest redox peak current and the largest electroactive surface area. This improvement is attributed to the unique hierarchical architecture of the composite. The porous NC framework not only provides a high specific surface area but also effectively disperses and stabilizes Bi_2MoO_6 NPs, preventing their agglomeration and thus maximizing the exposure of the catalytically active sites [56]. Moreover, the three-dimensional interconnected pore structure formed by the integration of the Bi_2MoO_6 and NC increases the electrode/electrolyte contact interface, providing more accessible regions for the $[Fe(CN)_6]^{3-/4-}$redox probe and significantly enhancing the interfacial charge storage and exchange capacity.

EIS measurements further corroborate these observations (Fig. 5B). The bare GCE exhibits the highest charge transfer resistance (R_c) of 63.7 Ω. In comparison, the R_c values for Bi_2MoO_6/GCE and NC/GCE decreased to 58.3 Ω and 32.1 Ω, respectively. Notably, the Bi_2MoO_6/NC/GCE displays the lowest R_{ct} (28.6 Ω), indicating that the composite forms an effective conductive network and substantially reduces the interfacial impedance to electron transfer. The apparent heterogeneous electron transfer rate (K_s) for each modified electrode was calculated using the equation: $K_s=RT/n^2F^2R_{ct}C$, where R is the gas constant (8.314 J mol^{-1} K^{-1}), T is the temperature (298 K), n is the number of electron transfers (n = 1), F is the Faraday constant (96485 C mol^{-1}), and C is the concentration of the redox probe. The resulting K_s values for bare GCE, Bi_2MoO_6/GCE, NC/GCE, and Bi_2MoO_6/NC/GCE are 8.35×10^{-7} cm s^{-1}, 9.13×10^{-7} cm s^{-1}, 1.66×10^{-6} cm s^{-1}, and 1.86×10^{-6} cm s^{-1}, respectively. These EIS results are excellent agreement with the CV data, confirming that the Bi_2MoO_6/NC/GCE offers superior electrical conductivity and a faster

electron transfer rate. This enhancement is primarily attributed to the continuous conductive network established by the NC matrix, which provides efficient pathway for electron transport. Furthermore, the synergistic conductive coupling between Bi_2MoO_6 and NC ensures effective electron transfer from the electrode surface to the target analyte during the electrochemical process, thereby laying the foundation for a rapid sensing response.

3.5 LSV responses of MAR at various electrodes

LSV analysis further substantiated the above findings (Figs. 5C-D). The i_{pa} values of MAR on bare GCE, Bi_2MoO_6/GCE, NC/GCE, and Bi_2MoO_6/NC/GCE were approximately 4.57 μA, 5.52 μA, 16.13 μA, and 24.6 μA, respectively. Pristine Bi_2MoO_6 alone conferred only a modest increase in peak current response, primarily due to its limited electrical conductivity. Although NC enhances mass transfer with its porous, molecular sieve-like architecture, its intrinsic conductivity remains moderate. In contrast, the Bi_2MoO_6/NC/GCE exhibited the most pronounced oxidation peak current response to MAR, substantially outperforming each individual component. This remarkable enhancement is attributed to a multidimensional synergistic effect. The porous NC framework selectively adsorbs and enriches MAR molecules, effectively reducing the diffusion distance [57]. Meanwhile, the uniformly dispersed Bi_2MoO_6 serves as highly active catalytic site, lowering the overpotential for MAR oxidation. The well-defined heterointerface formed between Bi_2MoO_6 and NC further optimizes the coupling between adsorption and catalysis, thereby enabling efficient electrocatalytic oxidation of MAR.

3.6 Electrochemical sensing properties

3.6.1 Calibration plot

Under optimal conditions, the analytical performance of Bi_2MoO_6/NC/GCE for MAR detection was evaluated by LSV across a series of concentrations (Fig. 5E). The oxidation peak current increased steadily with increasing MAR concentration in the range of 0.03 to 10 μM (Fig. 5F), yielding the linear regression equation i_{pa} (μA) = 7.958C (μM) + 0.4496 (R^2 = 0.9992). The sensitivity was calculated to be 7.958 μA $μM^{-1}$, and the limit of detection (LOD) was estimated to be 0.0045 μM. As summarized in Table 1, the overall sensing performance of the Bi_2MoO_6/NC/GCE is at least comparable to, or even exceeds, that of previously reported voltammetric sensors. The superior sensing performance is attributed to the integrated structural and electrochemical properties of the Bi_2MoO_6/NC composite. The high specific surface area and hierarchical porous architecture of NC facilitates efficient enrichment of MAR molecules at the electrode surface, thereby shortening the diffusion distance. Meanwhile, the abundant active sites–including metal centers from Bi_2MoO_6 and nitrogen-containing functional groups from NC–synergistically catalyzes the electron transfer process of MAR. This cooperative interplay enables the electrode to transduce MAR concentration signals into measurable current responses with high sensitivity and stability, underpinning its outstanding electrochemical sensing performance.

Table 1
A comparative evaluation of the analytical performance of Bi_2MoO_6/NC/GCE with previously reported methods for the electrochemical detection of MAR.

Detection Method	Sensing Material	LDR (μM)	LOD (μM)	Sensitivity	Stability (%)	Ref.
HPLC-UV	NA	6.9–48.3	0.69	2.184 μA μM^{-1}	NA	[58]
DPV	CuO	0.018-1.0	0.006	0.13 μA μM^{-1}	4 weeks (82.3%)	[59]
ITV	NA	1.0–50	1	3.21 μA μM^{-1}	NA	[60]
LC-UV	NA	0.50–1.2	NA	NA	NA	[61]
LSV	Bi_2MoO_6/NC	0.03-10	0.0045	7.958 μA μM^{-1}	2 weeks (74.6%)	This work

3.6.2 Anti-interfering assay

To evaluate the anti-interference capability of Bi_2MoO_6/NC/GCE, the LSV response was systematically examined in the presence of 2 μM MAR coexisting with equal concentrations of common interferents, including K^+, Fe^{3+}, Mn^{2+}, ascorbic acid (AA), dopamine (DA), gatifloxacin (GAT), norfloxacin (NFX), and lomefloxacin (LOM). As shown in Fig. 6A, C, no discernible oxidation peaks were observed for metal ions and certain small-molecule interferents, demonstrating high selectivity of the sensor toward these species. In contrast, GAT, NFX, LOM, and MAR each displayed characteristic oxidation peaks. Notably, the oxidation peak of MAR was well resolved from those of the other antibiotics, and its peak current intensity was markedly higher. This clear differentiation enables specific recognition of MAR, highlighting the exceptional “electronic structure recognition” capability of the composite [62]. The synergistic interplay between catalytic active centers of Bi_2MoO_6 (Bi^{3+}, Mo^{6+}) and the nitrogen-doped functional groups of NC creates a unique microenvironment capable of sensitively distinguishing subtle structural various among antibiotic molecules, such as substituents on the piperazine ring and the positions of fluorine atoms [63]. These structural disparities are ultimately manifested as distinct differences in both peak potential and peak current in voltammetric response, thereby enabling the selective identification of MAR.

When MAR was tested in mixture containing various interferents (Fig. 6B, D), the sensor exhibited highly stable response signals, with the relative peak current variations consistently below 2.0%. This further attests to the excellent anti-interference capability of the proposed sensor. Such robust performance is attributed to the hierarchical architecture and functional synergy of the composite material. The porous framework of NC confers a physical sieving effect that selectively enriches MAR molecules [64]. Additionally, the composite interface provides specific binding sites through hydrogen bonding, π-π

stacking, and other non-covalent interactions, which favor the preferential adsorption of MAR [65]. Collectively, these mechanisms ensure that the electrochemical interface remains predominantly governed by MAR even in the presence of high-concentration interfering substances. As a result, competing species are unable to effectively occupy active sites or generate overlapping signals, thereby guaranteeing the high precision and reliability in the detection of MAR.

3.6.3 Repeatability, reproducibility, and stability

The Bi_2MoO_6/NC/GCE demonstrated excellent reliability and durability, as confirmed by confirmed by comprehensive assessments of its reproducibility, repeatability, and long-term stability (Fig. 7). This outstanding performance originates from the robust sensing interface synergistically constructed between Bi_2MoO_6 and NC. In the reproducibility test, five independently fabricated electrodes exhibited highly consistent detection response toward MAR, with a relative standard deviation (RSD) of only 1.49% for the oxidation peak current. This uniformity is attributed to the the porous NC framework, which enables homogeneous loading and stable immobilization of Bi_2MoO_6 NPs, ensuring batch-to-batch consistency in the distribution of electroactive sites. Repeatability tests revealed that seven consecutive measurements using the same electrode yielded well-overlapped signals, indicating that the composite structure remains intact during electrochemical cycle. The conductive network of NC continuously facilitates efficient electron transport, while the Bi_2MoO_6 active center exhibit no significant deactivation or detachment. Long-term stability evaluation showed that the electrode retained 74.6% of its initial response after 14 days. The gradual performance decay is primarily ascribed to the slight dissolution of Bi_2MoO_6 during prolonged electrolysis. Nevertheless, the rigid carbon skeleton of NC effectively suppresses agglomeration and loss of active components, substantially delaying structural degradation. The integration of Bi_2MoO_6 and NC is not merely a physical mixture; rather, NC provides mechanical support and conductive stability to compensate for the intrinsic aggregation tendency and limited conductivity in Bi_2MoO_6, while Bi_2MoO_6 endows the interface with high catalytic activity. Together, they form a composite interface characterized by structural robustness, abundant active sites, and efficient electron transfer, thereby ensuring high precision, excellent reproducibility, and long-term stability for MAR sensing.

3.7 Real sample analysis

The applicability of the Bi_2MoO_6/NC/GCE for MAR detection in actual samples-namely tap water and milk-was evaluated (Fig. 8). No significant oxidation peaks were observed in the original unspiked samples, indicating negligible background MAR content and further confirming the high selectivity of the sensor. Upon spiking with MAR standards at concentration ranging from 0.5 to 5 μM, the oxidation peak current increased linearly with concentration, closely mirroring the behavior in the pure buffer system. This strong consistency suggests a stable electrode response mechanism with minimal matrix interference. The recoveries ranged from 96.0% to 100.6%, with an RSD below 5% (Table 2), underscoring the accuracy and repeatability of the proposed method for quantitative analysis.

The superior performance in complex matrices is attributed to the unique surface chemical microenvironment of the Bi_2MoO_6/NC composite interface, which preferentially and selectively adsorbs MAR molecules through specific interactions such as hydrogen bonding and π-π stacking. These interactions effectively suppress competitive adsorption from other components present in the sample matrix. As a result, the Bi_2MoO_6/NC/GCE not only offer high sensitivity and a broad linear range but also demonstrate robust anti-interference capability in real-world samples. Through the integrated functions of “screening-identification-catalysis” embedded in its architecture, the sensor enables accurate and stable detection of trace levels of MAR. These features highlight the considerable potential of this composite electrode for applications in environmental water quality monitoring and food safety analysis.

Table 2
Determination results for MAR residues in tap water and milk samples (n = 5).

Samples	Detected (μM)	Add (μM)	Found (μM)	RSD(%)	Recovery (%)
Tap water	ND	0.5	0.4825	0.03	96.5
		1	1.0015	0.23	100.1
		3	2.9668	1.05	98.9
milk	ND	5	4.9158	4.80	98.3
		0.5	0.4801	0.13	96.0
		1	1.006	0.15	100.6
		3	2.9706	0.77	99.0
		5	4.8919	0.40	97.8

ND: not detected.

4 Conclusion

In summary, a novel electrochemical sensor based on a Bi_2MoO_6/NC composite was successfully designed and constructed for the rapid and sensitive detection of MAR. The NC support, derived from waste coconut shells, features a high specific surface area (842.72 $m^2 g^{-1}$) and a hierarchical pore architecture, which facilitates efficient adsorption and enrichment of target molecules while providing a three-dimensional conductive network for accelerated electron transport. The uniform anchoring of flower-like Bi_2MoO_6 microspheres onto the NC framework creates a synergistic “adsorption-enrichment-catalysis” interface that significantly enhances the electrocatalytic oxidation of MAR. The optimized Bi_2MoO_6/NC/GCE exhibits outstanding analytical performance, including a wide linear range (0.03–10 μM), high sensitivity (7.958 μA $μM^{-1}$), low detection limit (0.0045 μM), excellent selectivity, and

remarkable reproducibility and stability. Practical application is demonstrated through spiked recovery tests in tap water and milk samples, with satisfactory recoveries (96.0–100.6%) and low RSDs, confirming the sensor's reliability for trace MAR detection in complex matrices. This study not only presents a cost-effective, efficient, and environmentally friendly sensing platform for on-site antibiotic monitoring but also offers a valuable strategy for designing multifunctional composite interfaces for the electrochemical detection of other emerging contaminants.

Declarations

CRediT authorship contribution statement

Yuan Jin: Conceptualization, Investigation, Methodology, Funding acquisition, writing-original draft. **Junyuan Song:** Investigation, Methodology, Formal analysis. **Nanke Ma:** Funding acquisition, Validation, Visualization. **Yonghui Xia:** Conceptualization, Methodology, Formal analysis, Writing-review & editing. **Guangli Li:** Conceptualization, Funding acquisition, Project administration, Supervision, Writing-review & editing.

Acknowledgements

This work was financially supported by the project of the Hunan Provincial Natural Science Foundation (2023JJ20024, 2023JJ40256 and 2020JJ6066), and Scientific Research Foundation of Hunan Province Education Department (24A0417 and 24C0292).

Conflict of Interests Statement

The authors declare that they have no conflict of interest.

Data Availability Statement

The data that support the findings of this study are available from the corresponding author upon reasonable request.

References

1. J. Ravichandran, B. S. Karthikeyan, A. Samal, Investigation of a derived adverse outcome pathway (AOP) network for endocrine-mediated perturbations, Science of The Total Environment, 826 (2022) 154112.
2. M. Rusch, A. Spielmeyer, J. Meißner, Efficient reduction of antibacterial activity and cytotoxicity of fluoroquinolones by fungal-mediated N-oxidation, Journal of agricultural and food chemistry, 65 (2017) 3118-3126.
3. Z. Li, X. Zhang, H. Fang, X. Lin, X. Dai, H. Liu, Photosynthetic toxicity of enrofloxacin on scenedesmus obliquus in an aquatic environment, Int. J. Environ. Res. Public Health 19 (2022) 5545.

4. J. Giannessi, L. De Marchi, V. Meucci, L. Intorre, G. Monni, M. Baratti, Veterinary fluoroquinolones as emerging contaminants in marine environments: In vitro study of biochemical responses in subcellular fractions of the Mediterranean mussel (Mytilus galloprovincialis), Heliyon, 10 (2024).
5. E. Shun-Mei, J. M. Zeng, H. Yuan, Y. Lu, R. X. Cai, Sub-inhibitory concentrations of fluoroquinolones increase conjugation frequency, Microbial pathogenesis, 114 (2018) 57-62.
6. N. S. Singh, N. Singhal, M. Kumar, Public health implications of plasmid-mediated quinolone and aminoglycoside resistance genes in Escherichia coli inhabiting a major anthropogenic river of India, Epidemiology & Infection, 150 (2022) e78.
7. M. Zhu, J. Chen, W. J. G. M. Peijnenburg, H. Xie, Z. Wang, S. Zhang, Controlling factors and toxicokinetic modeling of antibiotics bioaccumulation in aquatic organisms: A review, Critical Reviews in Environmental Science and Technology, 53 (2023) 1431-1451.
8. T. Hu, J. Zhang, X. Xu, Bioaccumulation and trophic transfer of antibiotics in the aquatic and terrestrial food webs of the Yellow River Delta, Chemosphere, 323 (2023) 138211.
9. Y. Wei, S. Zhang, X. Wu, Pollution and health risks of antibiotics in marine food webs from the South China Sea, Marine Pollution Bulletin, 225 (2026) 119280.
10. H. O. Khalifa , L. Shikoray, M. Y. I. Mohamed, Veterinary drug residues in the food chain as an emerging public health threat: Sources, analytical methods, health impacts, and preventive measures, Foods, 13 (2024) 1629.
11. Q. Yuan, Z. Zhang, Y. Chen, L. Hui, M. Wang, M. Xia, Origin and transformation of volatile organic compounds at a regional background site in Hong Kong: Varied photochemical processes from different source regions, Science of the Total Environment, 908 (2024) 168316.
12. M. Getahun, R. B. Abebe, A. K. Sendekie, Evaluation of antibiotics residues in milk and meat using different analytical methods, International journal of analytical chemistry, 1 (2023) 4380261.
13. R. Pratiwi, S. P. Ramadhanti, A. Amatulloh, Recent advances in the determination of veterinary drug residues in food, Foods, 12 (2023) 3422.
14. D. S. Gertner, J. P. Violi, D. P. Bishop, Lipid spectrum generator: a simple script for the generation of accurate in silico lipid fragmentation spectra, Analytical Chemistry, 95 (2023) 2909-2916.
15. X. Xu, Z. Jiang, X. Lai, B. Zhang, L. Wei, X. Cheng, Studies on the visual screening method for fluoroquinolones based on the chain reaction of gold nanoparticles and its application in milk samples, Microchemical Journal, 146 (2019) 600-605.
16. C. Weins. Overview of bioactivity-based analysis by HPTLC. Bridging the gap between cause and effect-HPTLC detection of bioactive compounds in the environment and in food, JPC–Journal of Planar Chromatography–Modern TLC, 21 (2008) 405-410.
17. M. A. Tantawy, A. M. Yehia, H. T. Elbalkiny, All-solid-state chip utilizing molecular imprinted polymer for erythromycin detection in milk samples: printed circuit board-based potentiometric system, Microchimica Acta, 190 (2023) 408.
18. W. B. Zhong, R. X. Li, J. Lv, Two isomeric In (III)-MOFs: unexpected stability difference and selective fluorescence detection of fluoroquinolone antibiotics in water, Inorganic Chemistry Frontiers, 7

(2020) 1161-1171.

19. K. F. Kayani, Portable smartphone-integrated ratiometric fluorescence probe for visual detection of mercury ions in environmental water with greenness evaluation, RSC advances, 15 (2025) 38612-38623.
20. M. Xie, Progress in graphene-based electrochemical sensors for antibiotic residue detection, Journal of Food Measurement and Characterization, 18 (2024) 6020-6034.
21. S. Jebril, Z. Fredj, A. A. Saeed, Nanomaterial-based electrochemical chemo (bio) sensors for the detection of nanoplastic residues: trends and future prospects, RSC Sustainability, 2 (2024) 832-851.
22. C. Li, W. Si, Y. Wu, C. Zhang, W. Lei, Q. Hao, Electrochemical Determination of Paracetamol at Poly (3-Methylthiophene)/Reduced Graphene Oxide Modified Glassy Carbon Electrode, Nano, 13 (2018) 1850104.
23. R. Nehru, S. Gnanakrishnan, C. W. Chen, Lignocellulosic carbon sheets-based hybrid electrochemical sensor for ultra-sensitive detection of chloramphenicol, Chemosphere, 370 (2025) 143911.
24. R. Umapathi, C. V. Raju, M. Safarkhani, Versatility of MXene based materials for the electrochemical detection of phenolic contaminants, Coordination Chemistry Reviews, 525 (2025) 216305.
25. H. Jin, C. Guo, X. Liu, J. Liu, A. Vasileff, Y. Jiao, Emerging two-dimensional nanomaterials for electrocatalysis, Chemical reviews, 118 (2018) 6337-6408.
26. L. Kulandaivel, J. W. Park, H. Jung, Exploiting synergistic effects of CoTe nanostructures and mesoporous graphene for enhanced OER electrocatalysis, International Journal of Hydrogen Energy, 141 (2025) 1-12.
27. H. Zhang, L. He, X. Zhang, Lattice oxygen and surface states dual modulation of manganese oxide with remarkably enhanced catalytic activity for toluene oxidation, Inorganic Chemistry Communications, 130 (2021) 108680.
28. Y. X. Wang, P .K. Tsao, M. Rinawati, Designing ZIF-67 derived NiCo layered double hydroxides with 3D hierarchical structure for Enzyme-free electrochemical lactate monitoring in human sweat, Chemical Engineering Journal, 427 (2022) 131687.
29. D. Wang, H. Shen, Guo L, Ag/Bi_2MoO_{6-x} with enhanced visible-light-responsive photocatalytic activities via the synergistic effect of surface oxygen vacancies and surface plasmon, Applied Surface Science, 436 (2018) 536-547.
30. W. D. Adane, B. S. Chandravanshi, N. Getachew, A cutting-edge electrochemical sensing platform for the simultaneous determination of the residues of antimicrobial drugs, rifampicin and norfloxacin, in water samples, Analytica Chimica Acta, 1312 (2024) 342746.
31. M. Jin, S. Lu, L. Ma, M. Gan, One-step synthesis of in situ reduced metal Bi decorated bismuth molybdate hollow microspheres with enhancing photocatalytic activity, Applied Surface Science, 396 (2017) 438-443.

32. M. Liu, Z. Liu, C. Xiang, MoS_2-$CuCo_2S_4$ nanosheets with a honeycomb structure formed on Ni foam: An efficient electrocatalyst for hydrogen evolution reaction, Journal of Alloys and Compounds, 988 (2024) 174300.
33. C. Zhou, J. Wang, X. Yan, Vertical MoS_2 nanosheets arrays on carbon cloth as binder-free and flexible electrode for high-performance all-solid-state symmetric supercapacitor, Ceramics International, 45 (2019): 21534-21543.
34. Y. Bae, L. Li, K. Yang, Fluorination of an N, N, N', N'-Tetraphenylbenzidine Derivative as a Dopant-Free Hole-Transporting Material for Moisture-Resistant Perovskite Solar Cells, ACS Applied Energy Materials, 4 (2021) 10459-10467.
35. M. Govindasamy, Z. A. ALOthman, R. A. Alshgari, Highly efficient electrocatalytic oxidation of hexestrol based on bismuth molybdenum oxide nanoparticle/graphene oxide nanosheets modified screen printed electrode, Journal of Environmental Chemical Engineering, 11 (2023) 109680.
36. R. Chen, W. Zhou, W. Qu, A novel hierarchical nanostructured S-scheme RGO/Bi_2MoO_6/Bi_2WO_6 heterojunction: excellent photocatalytic degradation activity for pollutants, Applied Surface Science, 588 (2022) 152788.
37. H. Wang, Y. Zhong, M. Li, Self-Grown Carbon Nanotube Encapsulated Co Nanoparticle Compound Fe-Nx/Mesoporous Carbon as Bi-Functional Electrocatalyst to Drive Efficient Electrochemical Overall Water Splitting, Chemistry-an Asian journal, 21 (2026) e70527.
38. J. Yan, L. Wang, Y. Qin, W. Kang, G. Yang, An efficient charge extraction strategy for high-performance piezoelectric nanogenerators via a 3D nanostructured conductive network, Nano Energy, (2025) 111037.
39. H. Wang, C. Srinivasakannan, M. Liu, Microwave-assisted synthesis of porous graphitized biochar as a super sorbent for tetracycline separation, Biochemical Engineering Journal, 205 (2024) 109291.
40. Y. Fang, Y. Li, F. Zhou, P. Gu, J. Liu, D. Chen, An efficient photocatalyst based on black TiO_2 nanoparticles and porous carbon with high surface area: degradation of antibiotics and organic pollutants in water, ChemPlusChem, 84 (2019) 474-480.
41. A. Longo, D. Mauri, C. J. Sahle, Shaping the empty Carbon nanocubes: the role of Nitrogen. Insight from X-Ray Raman Scattering Spectroscopy at the N K-edge, Carbon, (2025) 120341.
42. D. Wu, Y. Yang, J. Liu, Y. Zheng, Plasma-modified N/O-doped porous carbon for CO_2 capture: an experimental and theoretical study, Energy & Fuels, 34 (2020) 6077-6084.
43. K. Moorthi, J. Yesuraj, K. Kim, S. Mohan, Electrochemical performance of chemically integrated N-doped carbon dots/Bi_2MoO_6 nanocomposites for symmetric supercapacitors, Energy & Fuels, 37 (2023) 6841-6853.
44. C. Zhou, R. Zhang, Y. Rong, Y. Yang, X. Jiang, Facile synthesis of hierarchically porous Ni–N–C for efficient CO_2 electroreduction to CO, ACS Applied Materials & Interfaces, 15 (2023): 42585-42593.
45. J. Liang, T. Qu, X. Kun, Y. Zhang, S. Chen, Y. C. Cao, Microwave assisted synthesis of camellia oleifera shell-derived porous carbon with rich oxygen functionalities and superior supercapacitor

performance, Applied Surface Science, 436 (2018) 934-940.
46. L. Tong, T. Wang, Y. Chen, G. Lin, L. He, X. Liu, Nitrogen self-doped porous lamellar carbon with superior electrochemical performance, Diamond and Related Materials, 134 (2023) 109787.
47. Q. Li, X. Xu, J. Chen, Z. Yin, Y. Zhang, F. Ma, S. Cao, The Controlled Synthesis of Flower-Like TiO_2 Nanosheets with Enhanced Photocatalytic Performance, Journal of Cluster Science, 35 (2024) 1507-1520.
48. S. Xun, Q. Ti, Z. Jiao, L. Wu, M. He, L. Chen, H. Li, Dispersing TiO_2 nanoparticles on graphite carbon for an enhanced catalytic oxidative desulfurization performance, Industrial & Engineering Chemistry Research, 59 (2020) 18471-18479.
49. Y. Jin, F. Han, D. Tong, X. Song, D. Wang, T. Wang, G. Xu, Coral-like cobalt/nitrogen-doped porous carbon synergized with MnO_2 for ultrasensitive electrochemical detection of luteolin in floral teas, Food Chemistry, 495 (2025) 146385.
50. M. Govindasamy, Z. A. ALOthman, R. A. Alshgari, Highly efficient electrocatalytic oxidation of hexestrol based on bismuth molybdenum oxide nanoparticle/graphene oxide nanosheets modified screen printed electrode, Journal of Environmental Chemical Engineering, 11 (2023) 109680.
51. M. Ayiania, M. Smith, A. J. R. Hensley, L. Scudiero, J. S. McEwen, M. Garcia-Perez, Deconvoluting the XPS spectra for nitrogen-doped chars: An analysis from first principles, Carbon, 162 (2020) 528-544.
52. D. Goodacre, M. Blum, C. Buechner, V. Jovic, J. B. Franklin, S. Kittiwatanakul, K. E. Smith, Methanol Adsorption on Vanadium Oxide Surfaces Observed by Ambient Pressure X-ray Photoelectron Spectroscopy, The Journal of Physical Chemistry C, 125 (2021): 23192-23204.
53. M. Voigt, J. M. Dluziak, N. Wellen, M. Jaeger, Mechanistic study of the electrochemical oxidation of fluoroquinolones: Ciprofloxacin, danofloxacin, enoxacin, levofloxacin and lomefloxacin, Chemosphere, 355 (2024) 141763.
54. Y. Huang, K. Liu, S. Kan, Highly dispersed Fe-Nx active sites on Graphitic-N dominated porous carbon for synergetic catalysis of oxygen reduction reaction, Carbon, 171 (2021) 1-9.
55. Z. Deng, M. Gong, Z. Gong, X. Wang, Mesoscale mass transport enhancement on well-defined porous carbon platform for electrochemical H_2O_2 synthesis, Nano Letters, 22 (2022) 9551-9558.
56. H. Elhaes, M. A. Ibrahim, Investigating the electronic properties of graphene oxide functionalized with benzoic acid, Scientific Reports, 15 (2025) 38105.
57. S. Gao, L. Zhang, H. Yu, Palladium-encapsulated hollow porous carbon nanospheres as nanoreactors for highly efficient and size-selective catalysis, Carbon, 175 (2021) 307-311.
58. K. R. W. Oliveira, R. A. Sversut, A. K. Singh, M. S. Amaral, N. M. Kassab, Development and validation of HPLC assay method for marbofloxacin determination in veterinary chewable tablets, Acta Chromatographica, 31 (2019) 291-293.
59. Hendawy, A. Hassan, E. Khaled, Voltammetric Determination of Marbofloxacin at Carbon Paste Sensor Integrated with Copper Oxide Nanoparticles, Electroanalysis, 35 (2023) e202200402.

60. K. Rudnicki, L. Poltorak, S. Skrzypek, E. J. Sudhölter, Ion transfer voltammetry for analytical screening of fluoroquinolone antibiotics at the water-1.2-dichloroethane interface, Analytica Chimica Acta, 1085 (2019) 75-84.
61. S. De Robertis, L. Elviri, A. Bianchera, R. Bettini, Stability-indicating liquid chromatography–spectrophotometric UV method for the simultaneous determination of marbofloxacin, dexamethasone and clotrimazole in a liquid pharmaceutical dosage form, Chromatographia, 78 (2015) 1299-1304.
62. H. Bai, Q. Zhang, X. Zhou, J. Chen, Z. Chen, Z. Liu, J. Wang, Removal of fluoroquinolone antibiotics by adsorption of dopamine-modified biochar aerogel, Korean Journal of Chemical Engineering, 40 (2023) 215-222.
63. S. Shi, C. Zhou, A. Chen, Bi_2MoO_6/MWCNTs-COOH/GCE electrochemical probe for ultrasensitively and selectively detecting antibiotic norfloxacin, Chemosphere, 364 (2024) 143139.
64. M. Singh, H. Gupta, P. Bedi, C. P. Pradeep, Transformation of a Polyoxometalate Precursor into Carbon Doped Bismuth Molybdate Nanosheets for the Visible Light Photocatalytic Degradation of Aqueous Pollutants, ACS Applied Nano Materials, 7 (2024) 17596-17610.
65. M. Zhao, C. R. Zhang, L. Zhang, Z. Chen, R. P. Liang, W. Jiang, J. D. Qiu, A zwitterionic covalent organic framework with multiple active sites for selective and efficient adsorption of ciprofloxacin via synergistic interactions, Applied Surface Science, (2025) 165777.

Figures

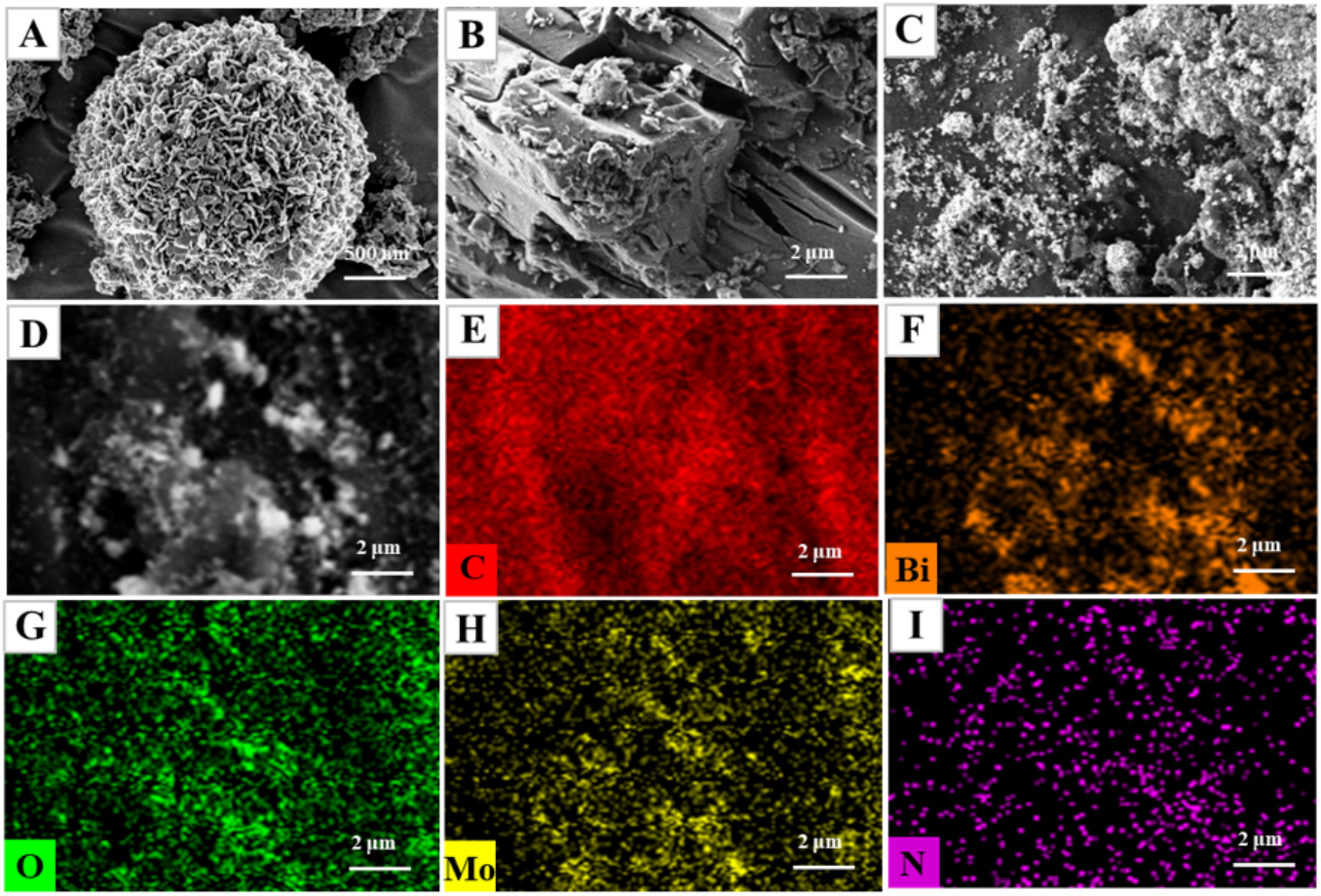


Figure 1

SEM images of (A) Bi_2MoO_6, (B) NC, and (C) Bi_2MoO_6/NC. (D-I) Elemental mapping images of C, Bi, O, Mo, and N elements of Bi_2MoO_6/NC.

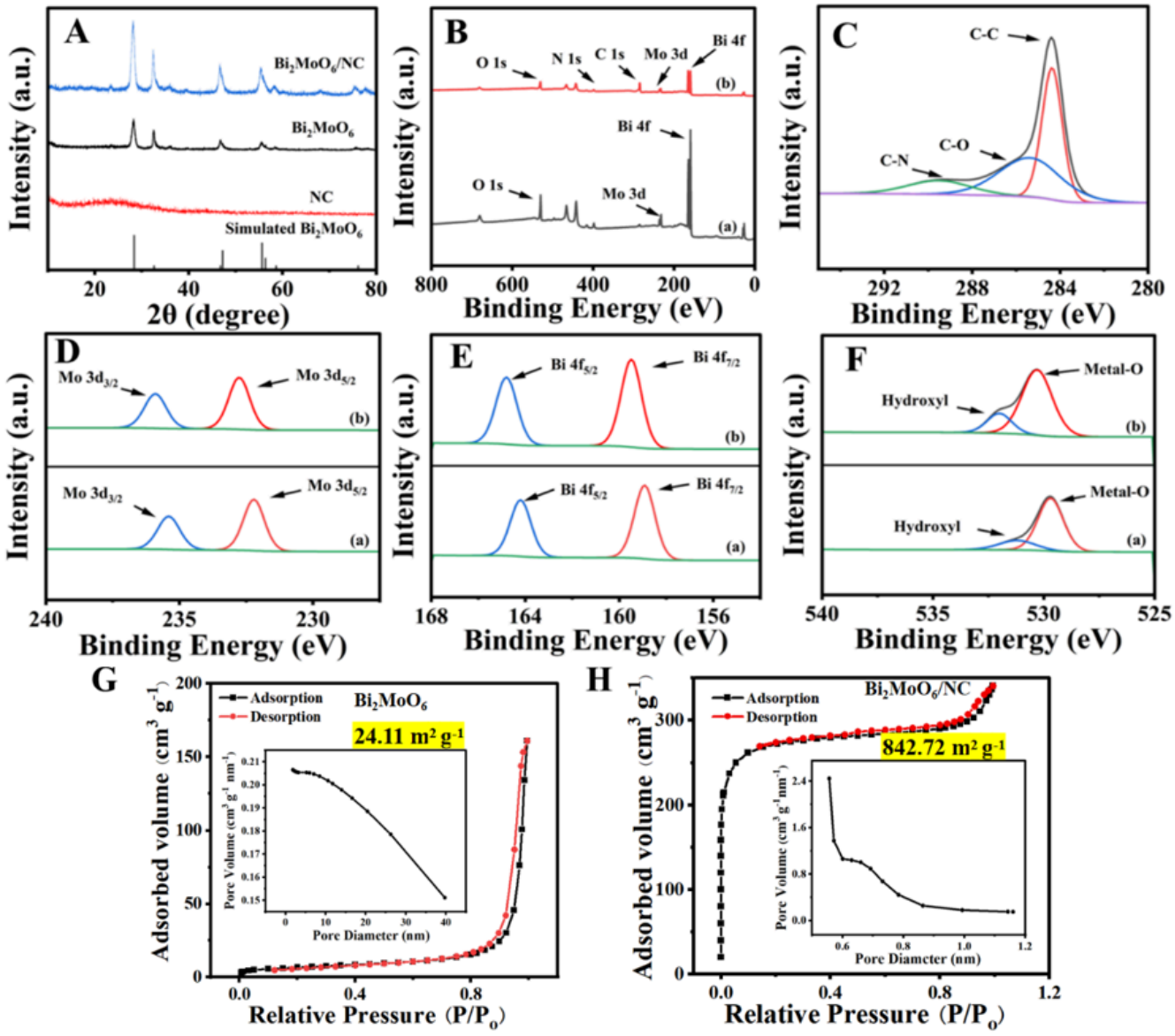


Figure 2

(A) XRD patterns of NC, Bi_2MoO_6, and Bi_2MoO_6/NC. (B) Survey XPS spectra of (a) Bi_2MoO_6 and (b) Bi_2MoO_6/NC. High-resolution XPS spectra of (C) C 1s, (D) Mo 3d, (E) Bi 4f, and (F) O 1s. Nitrogen adsorption and desorption isotherms of (G) Bi_2MoO_6 and (H) Bi_2MoO_6/NC, and insets show the corresponding pore size distributions.

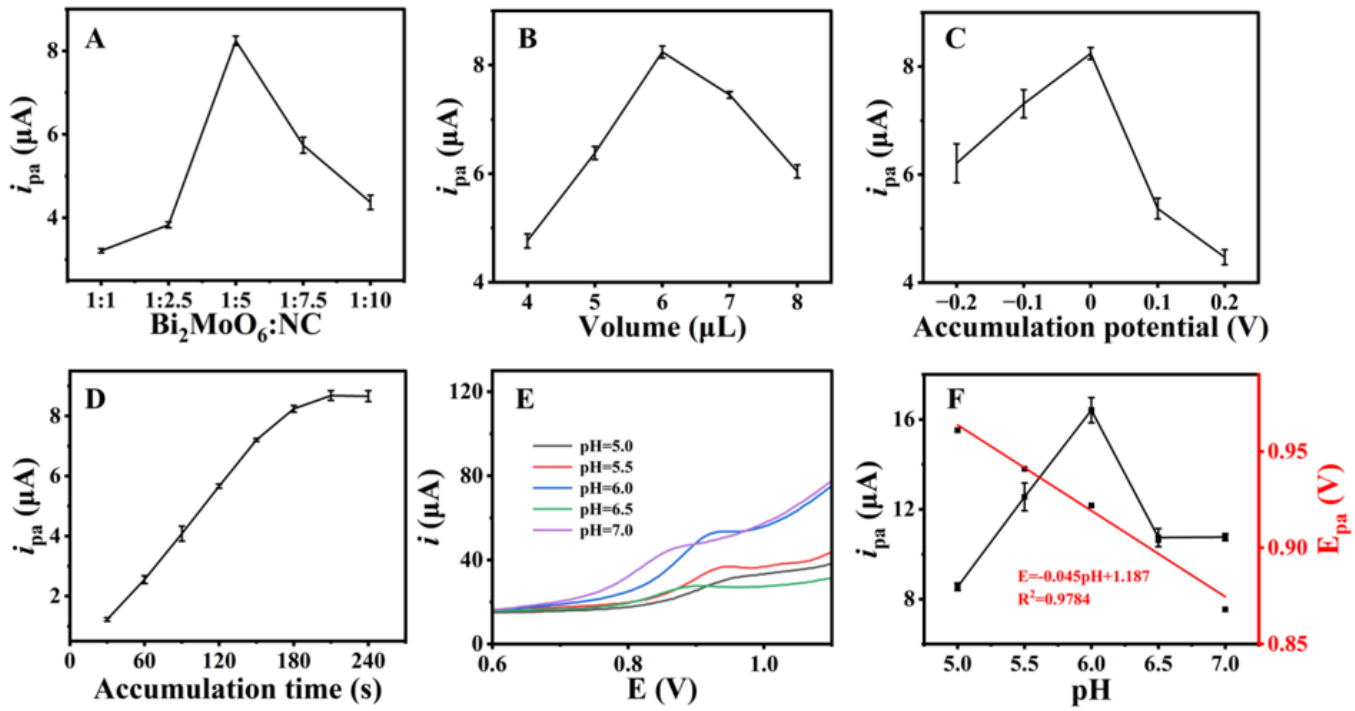


Figure 3

Influences of (A) Bi_2MoO_6/NC mass ratio; (B) loading volume of Bi_2MoO_6/NC; (C) accumulation potential and (D) accumulation time on the response peak current of MAR; (E) LSV curves of 10 μM MAR at different pH values, and (F) associated linear plots of i_{pa}(MAR) and E_{pa}(MAR) versus buffer pH.

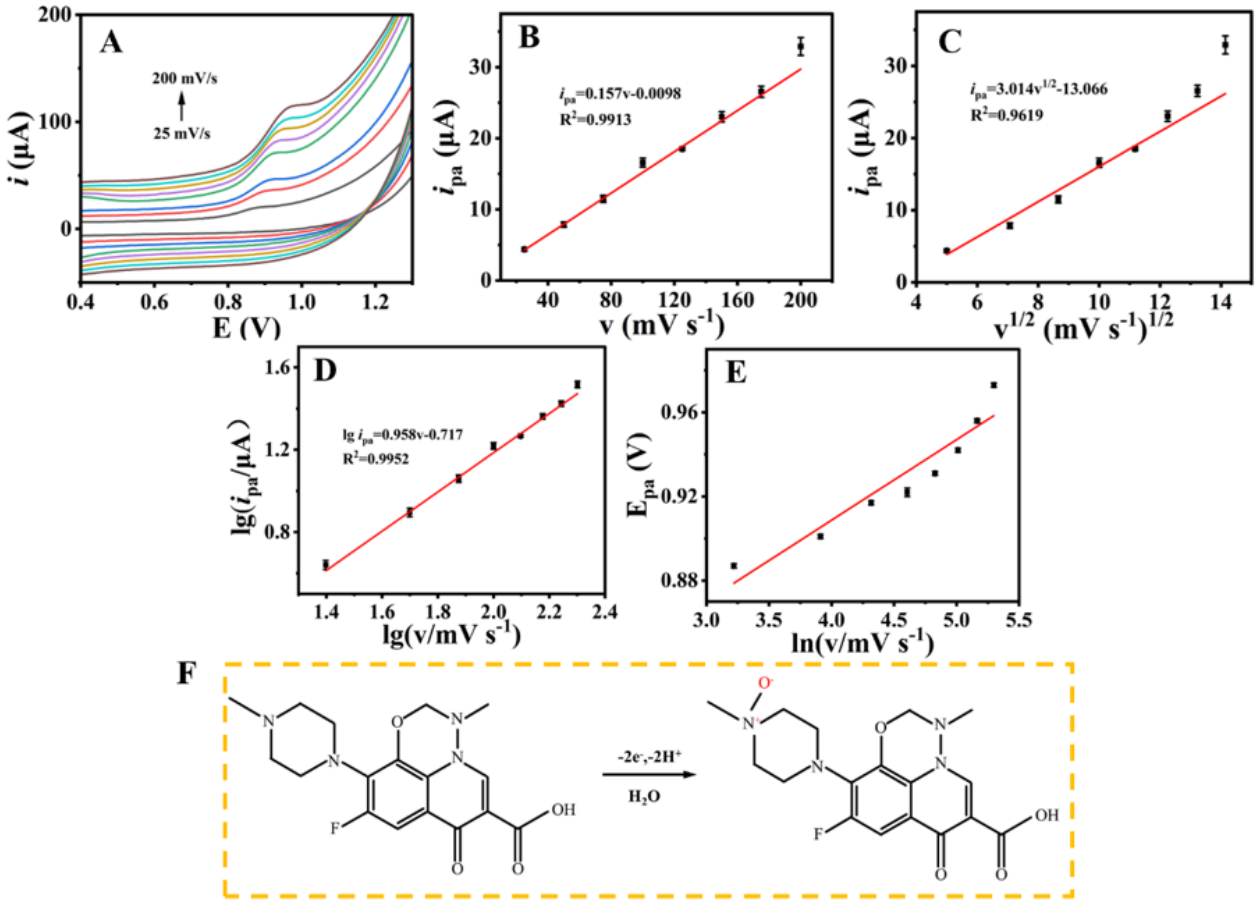


Figure 4

Electrooxidation mechanism of MAR on Bi_2MoO_6/NC/GCE. (A) CV curves of 1.0 μM MAR at different scan rates (*v*). (B) Linear relationship between i_{pa}(MAR) and *v*. (C) Linear relationship between i_{pa} and $v^{1/2}$. (D) Linear relationship between lgi_{pa} and lg*v*. (E) Linear relationship between E_{pa} and ln*v*. (F) Proposed electrooxidation mechanism of MAR on Bi_2MoO_6/NC/GCE.

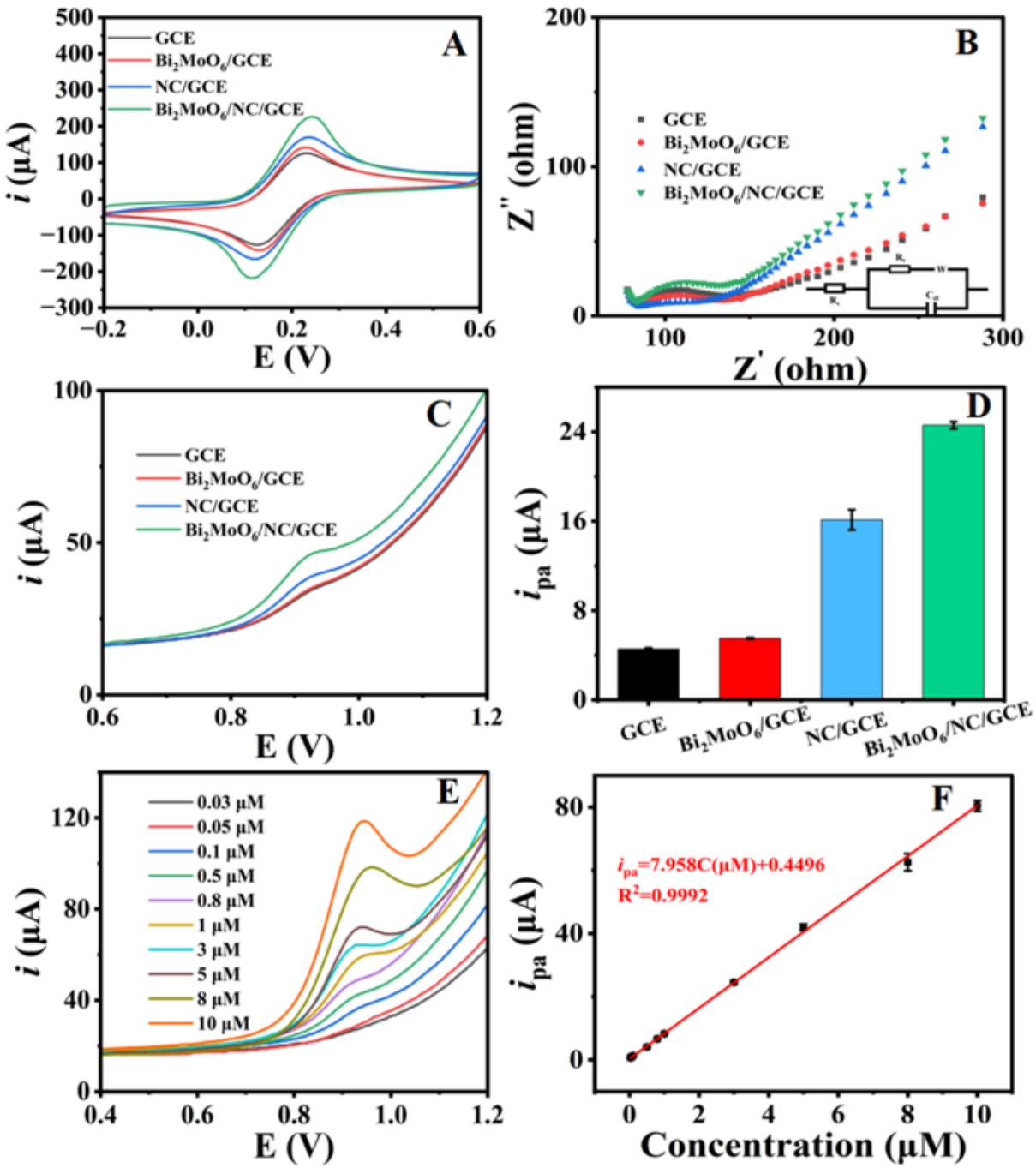


Figure 5

(A) CV diagrams and (B) Nyquist plot for GCE, Bi_2MoO_6/GCE, NC/GCE and Bi_2MoO_6/NC/GCE electrode systems in a 0.1 M KCl solution containing 5 mM $[Fe(CN)_6]^{3-/4-}$; (C) LSV curves and (D) corresponding i_{pa}(MAR) of different electrode recorded in 0.1 M PBS (pH 6.0) solution containing 1.0 μM of MAR; (E) LSV plots of MAR recorded on the Bi_2MoO_6/NC/GCE in 0.1 M PBS (pH 6.0) solution containing different concentrations of MAR; (F) Linear plot of i_{pa}(MAR) versus MAR concentration.

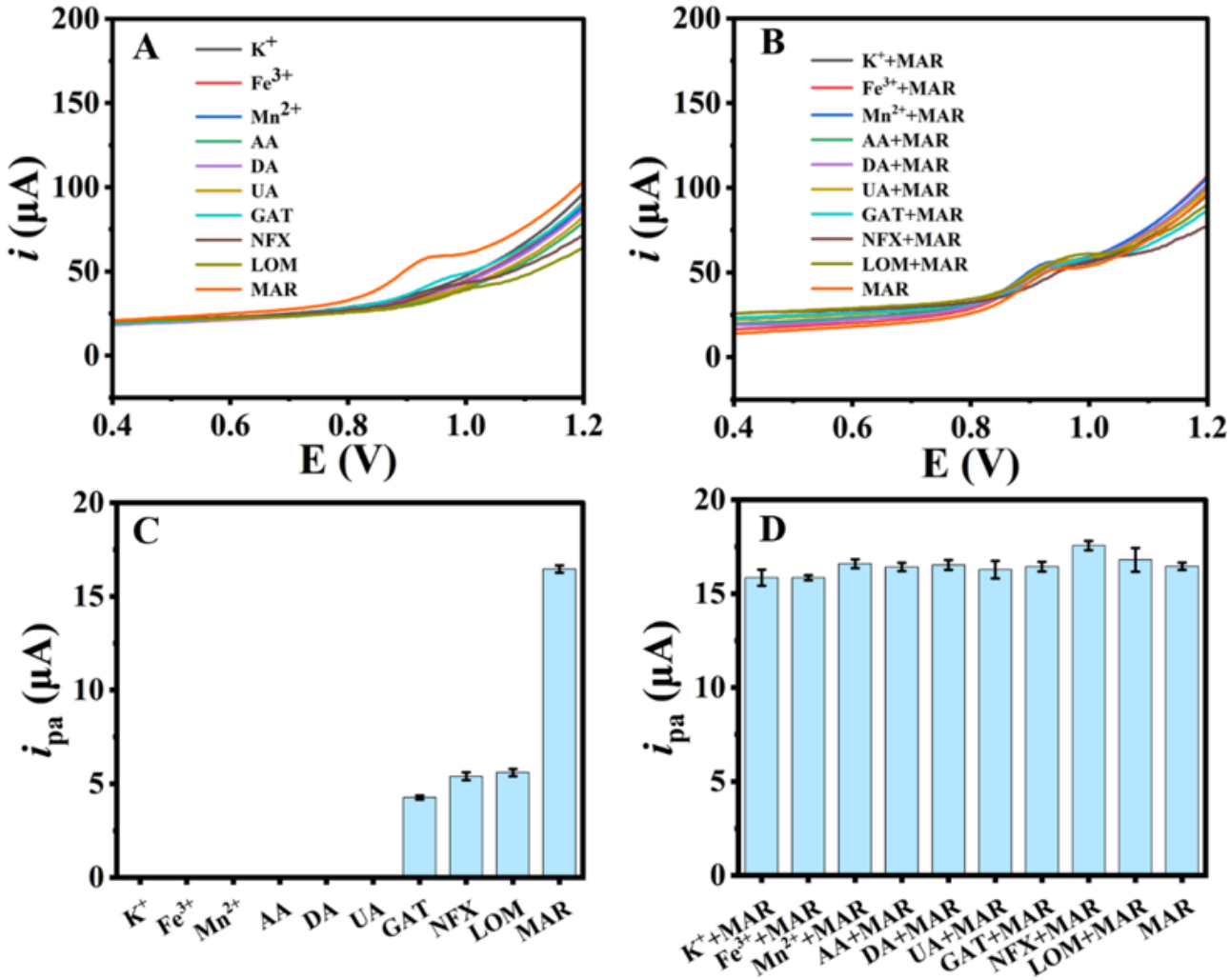


Figure 6

(A) LSV curves and (B) corresponding i_{pa} of MAR (1.0 μM), KCl (100 μM), $MnCl_2$ (100 μM), Fe $(NO_3)_3$ (100 μM), AA (5.0 μM), DA (5.0 μM), UA (5.0 μM), GAT (5.0 μM), NFX (5 μM), and LOM (5.0 μM); (C) LSV plots and (D) corresponding i_{pa} of 1.0 μM MAR in the presence of these potential interfering substances.

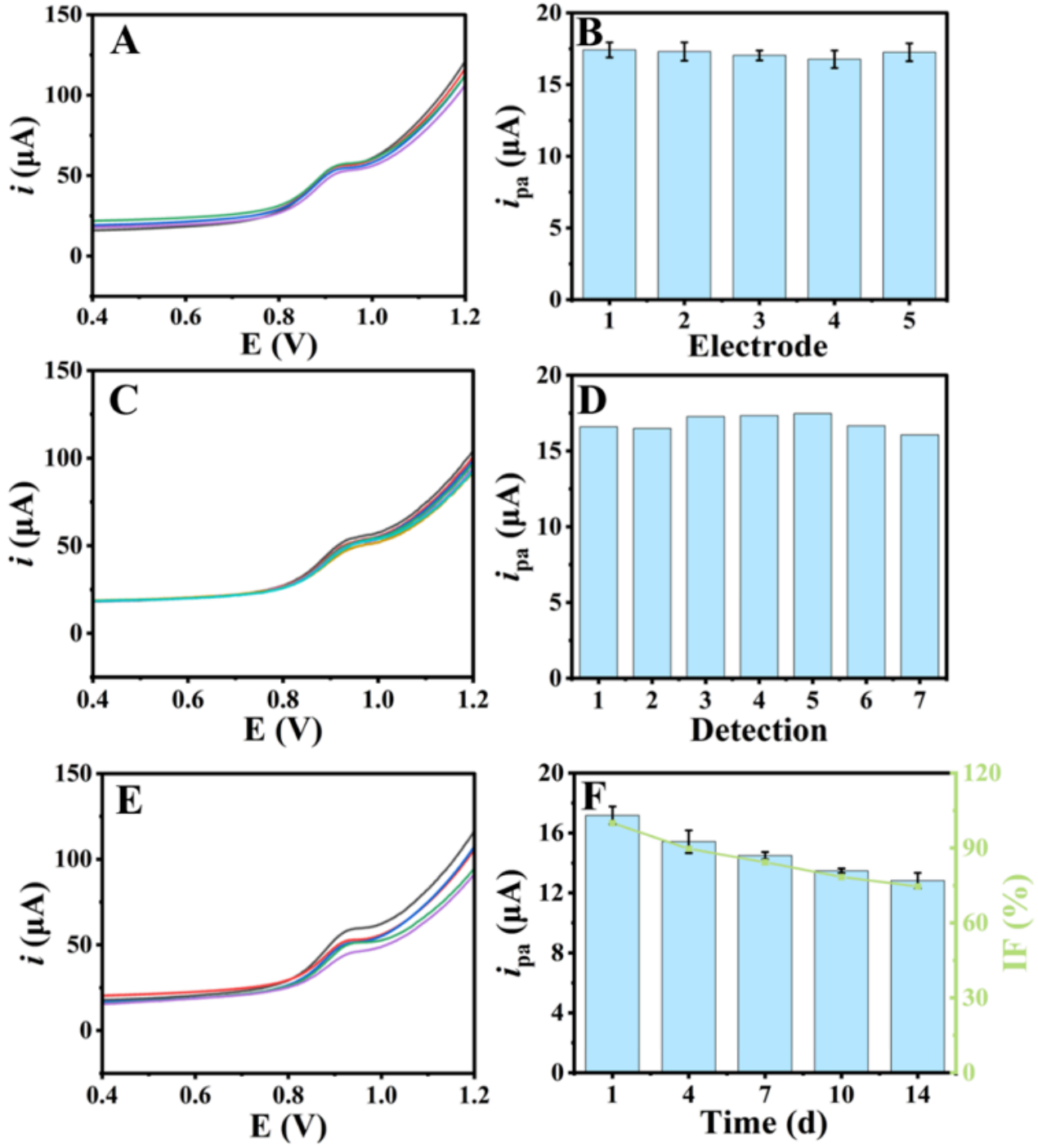


Figure 7

(A) LSV curves and (D) respective peak current responses of parallel detections of 1.0 μM MAR using five independent Bi_2MoO_6/NC/GCEs. (B) LSV curves and (E) respective peak current responses of seven consecutive detections of 1.0 μM MAR using the same Bi_2MoO_6/NC/GCE. (C) LSV curves and (F) variations in the peak current responses of 1.0 μM MAR over a period of 14 days.

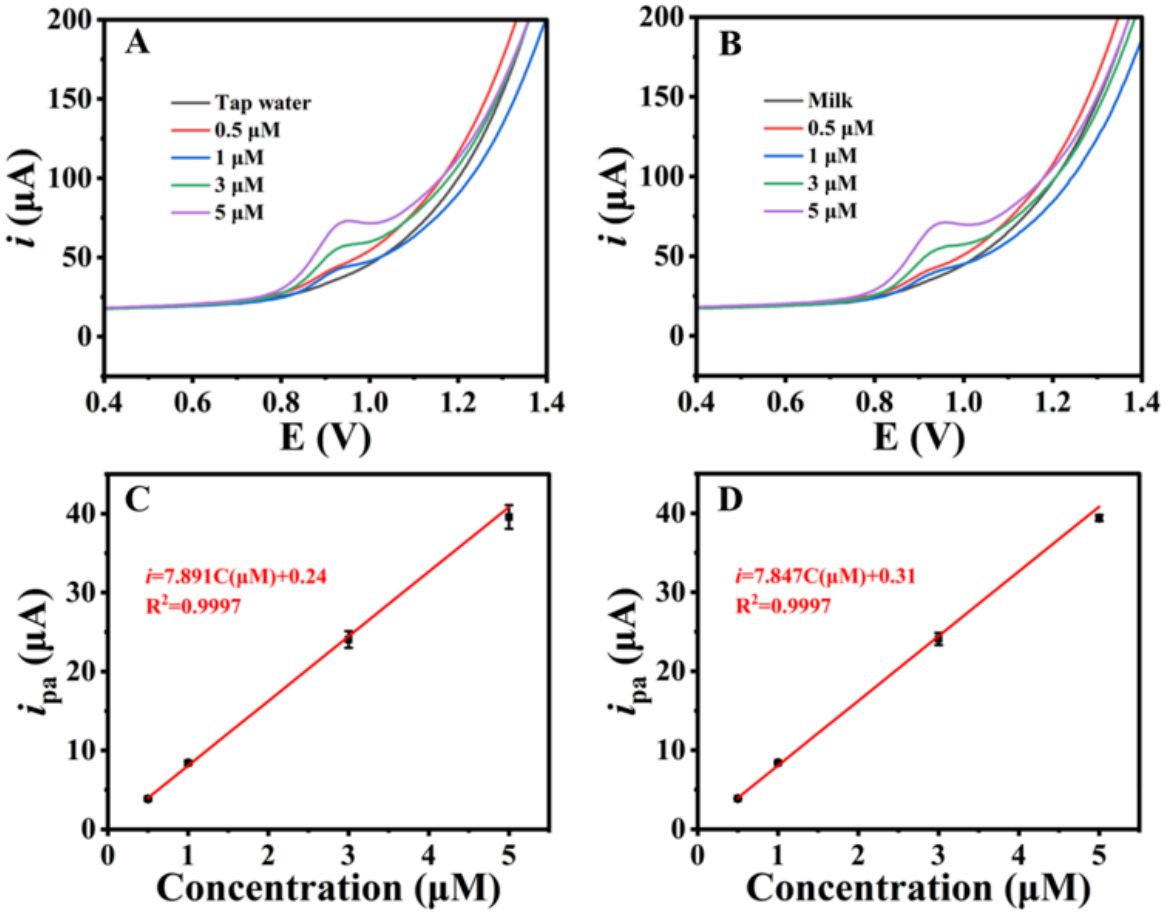


Figure 8

Real sample analysis of MAR in tap water and milk. (A-B) LSV plots of tap water and milk spiked with different concentrations of MAR. (C-D) Linear plots of anodic peak current of MAR against the concentration of MAR in tap water and milk.